Relaxometric studies of gadolinium-functionalized perfluorocarbon nanoparticles for MR imaging

CONTRAST MEDIA & MOLECULAR IMAGING

Received: 5 March 2012, Revised: 23 February 2013, Accepted: 10 March 2013, Published online in Wiley Online Library

(wileyonlinelibrary.com) DOI: 10.1002/cmmi.1541

Relaxometric studies of gadolinium-functionalized perfluorocarbon nanoparticles for MR imaging

Anke de Vries[a], Rik Moonen[a], Muhammed Yildirim[b], Sander Langereis[b], Rolf Lamerichs[b], Jeroen A. Pikkemaat[b], Simona Baroni[c], Enzo Terreno[c], Klaas Nicolay[a], Gustav J. Strijkers[a] and Holger Grüll[a,b]*

Fluorine MRI (^{19}F MRI) is receiving an increasing attention as a viable alternative to proton-based MRI (^{1}H MRI) for dedicated application in molecular imaging. The ^{19}F nucleus has a high gyromagnetic ratio, a 100% natural abundance and is furthermore hardly present in human tissues allowing for hot spot MR imaging. The applicability of ^{19}F MRI as a molecular and cellular imaging technique has been exploited, ranging from cell tracking to detection and imaging of tumors in preclinical studies. In addition to applications, developing new contrast materials with improved relaxation properties has also been a core research topic in the field, since the inherently low longitudinal relaxation rates of perfluorocarbon compounds result in relatively low imaging efficiency. Borrowed from ^{1}H MRI, the incorporation of lanthanides, specifically Gd(III) complexes, as signal modulating ingredients in the nanoparticle formulation has emerged as a promising approach to improvement of the fluorine signal. Three different perfluorocarbon emulsions were investigated at five different magnetic field strengths. Perfluoro-15-crown-5-ether was used as the core material and Gd(III)DOTA–DSPE, Gd(III)DOTA–C6–DSPE and Gd(III)DTPA–BSA as the relaxation altering components. While Gd(III)DOTA–DSPE and Gd(III)DOTA–C6–DSPE were favorable constructs for ^{1}H NMR, Gd(III)DTPA–BSA showed the strongest increase in $^{19F}R_1$. These results show the potential of the use of paramagnetic lipids to increase $^{19F}R_1$ at clinical field strengths (1.5–3 T). At higher field strengths (6.3–14 T), gadolinium does not lead to an increase in $^{19F}R_1$ compared with emulsions without gadolinium, but leads to an significant increase in $^{19F}R_2$. Our data therefore suggest that the most favorable situation for fluorine measurements is at high magnetic fields without the inclusion of gadolinium constructs. Copyright © 2014 John Wiley & Sons, Ltd.

Keywords: ^{19}fluorine; MRI; relaxometry; gadolinium; nanoparticles; perfluorocarbon

1. INTRODUCTION

MRI is a powerful molecular imaging tool as it provides high-resolution images and excellent soft-tissue contrast without the need for ionizing radiation. Quantitative molecular imaging of cellular disease markers has been found to be essential for the characterization of disease processes. A promising quantitative technique is ^{19}F MR imaging. Among the advantages of ^{19}F MRI is the fact that the ^{19}F nucleus has a 100% natural abundance, a nuclear spin of ½ and a sensitivity comparable to that of ^{1}H-NMR. The lack of background signal enables quantification of the fluorine concentration. However, the sensitivity of ^{19}F MRI remains a challenge as the local ^{19}F concentration by far cannot approach the ^{1}H content of the human body. Therefore, ^{19}F MRI contrast agents that provide high local ^{19}F densities are required to reach detectable ^{19}F concentrations. Over the last decade, perfluorocarbon nanoparticles have demonstrated their potential for quantitative molecular imaging of fibrin-targeted clots in atherosclerosis (1), $\alpha_v\beta_3$-targeting of angiogenesis in diseased aortic valve leaflets (2) and VCAM-1 targeted renal inflammation (3). Moreover, perfluorocarbon (PFC) nanoparticles have been investigated for use in cell trafficking enabling quantitative assessment of the biodistribution of labeled neural stem cells (4) and T-cells (5–7). Furthermore, quantitative ^{19}F MRI of perfluorocarbons has been explored for mapping of tumor oxygenation (8,9).

Several approaches to increase the sensitivity of ^{19}F MR at the imaging site of interest have been studied. For instance, it has been shown that the vicinity of the lanthanide gadolinium ion, Gd(III), significantly increases the fluorine longitudinal relaxation rate [$^{19F}R_1$ (s^{-1})] (10,11). The influence of a gadolinium-functionalized lipid [Gd(III)DTPA–BOA] in the perfluoro-15-crown-5-ether (PFCE) emulsion monolayer on the $^{19F}R_1$ and $^{19F}R_2$ was recently investigated, showing that the fluorine relaxation $^{19F}R_1$ rate not only depends on the Gd concentration but also decreased upon increased field

* *Correspondence to: Holger Grüll, Biomedical NMR, Department of Biomedical Engineering, Eindhoven University of Technology, Eindhoven, The Netherlands. E-mail: h.gruell@tue.nl*

a *A. Vries, R. Moonen, K. Nicolay, G. J. Strijkers, H. Grüll*
Biomedical NMR, Department of Biomedical Engineering, Eindhoven University of Technology, Eindhoven, The Netherlands

b *M. Yildirim, S. Langereis, R. Lamerichs, J. A. Pikkemaat, H. Grüll*
Department of Minimally Invasive Healthcare, Philips Research, Eindhoven, The Netherlands

c *S. Baroni, E. Terreno*
Dipartimento di Chimica IFM and Molecular Imaging Center, Torino, Italy

strength and vice versa for $^{19F}R_2$ (12). Intuitively one would assume that the Gd incorporated in the Gd(III)DTPA–BOA lipid is situated on the outside of the nanoparticle monolayer as the Gd(III)DTPA head group is a hydrophilic construct and not soluble in PFCE. The results of Neubauer *et al.*, however, suggest that the paramagnetic center is in close enough proximity of ^{19}F to still increase relaxivity of the PFCE inside the emulsion. Taking the Solomon–Bloembergen–Morgan theory of relaxivity as a basis, the underlying mechanism must be related to outer sphere relaxation as any direct contact between the fluorinated molecules inside the emulsion droplet and the Gd-chelate head group is prohibited by the lipid monolayer. In addition, the observed alteration of ^{19}F relaxation rate must increase with the amount of Gd content in the monolayer and decrease with increasing volume of the emulsion droplet. The latter is the consequence of the increasing distance each fluorinated molecule has to diffuse inside the emulsion droplet to get close to the surface layer in order to feel the dipolar interactions with the paramagnetic head-group. The above intuitive rational was worked out recently in more detail by Hu *et al.*, giving a theoretical model and first experimental data (13).

An increase in sensitivity for ^{19}F MRI would be beneficial for ^{19}F applications in clinical practice. Gd-functionalized nanoparticles are currently investigated for use in molecular MR imaging applications as they create an increased proton R_1 and allow a delineation of the diseased tissue using proton MR. US Food and Drug Administration approval for all Gd-related nanoparticulate contrast agents is, however, complicated as they are taken up via the reticulo endothelial system, which may lead to a prolonged retention time of Gd-compounds *in vivo*. The latter may lead to nephrogenic systemic fibrosis (NSF), which is mostly observed in patients with impaired renal excretion after injection of Gd contrast agents based on a bisamide chelate. Most likely, the lower stability of Gd bisamide complexes compared to DTPA or DOTA complexes in combination with the long body retention time leads to considerable transmetallation of Gd inducing toxicity (14–16). As Gd–DOTA constructs show a much higher kinetic stability and lower transmetallation rate than Gd(III)DTPA–bisamide constructs (17,18), it would be the more favorable chelate to incorporate in the lipid bilayer of fluorine nanoparticles. Whether the influence on the relaxation rate of fluorine persists when Gd(III)DOTA is used instead of Gd(III)DTPA remains to be investigated.

Here, we investigate the influence of three gadolinium–lipids on the water proton relaxivities and fluorine relaxation rates ($^{19F}R_1$ and $^{19F}R_2$) of PFCE nanoparticles (Fig. 1). Gd(III)DOTA–DSPE, Gd(III)DOTA–C6–DSPE and Gd(III)DTPA–BSA are employed in our formulations as relaxation agents, investigating not only the difference between Gd(III)DOTA–DSPE and Gd(III)DTPA–BSA, but also whether an aliphatic spacer of approximately 6 Å [Gd(III)DOTA–C6–DSPE] alters the influence of Gd on $^{19F}R_1$ and $^{19F}R_2$. These three fluorine emulsions (FE) will from here on be referred to as FE–DOTA, FE–C6–DOTA and FE–DTPA. ^1H NMRD measurements were performed on all Gd-constructs to define the positioning and movement of gadolinium on the constructs. All fluorine $^{19F}R_1$ and $^{19F}R_2$ measurements were performed at five different field strengths and were compared with the results of two controls, being a PFCE emulsion without any Gd incorporated (referred to as FE) and a PFCE emulsion having Gd only present in the aqueous solution as Gd(III)HPDO3A (further referred to as FE + HPDO3A).

2. METHODS

2.1. Materials

1,2-Distearoyl-*sn*-glycero-3-phosphocholine (DSPC), cholesterol and 1,2-distearoyl-*sn*-glycero-3-phosphoethanolamine-*N*-[methoxy(−polyethyleneglycol)-2000] (DSPE-PEG_{2000}) were obtained from Lipoid (Germany). 1,2-Dipalmitoyl-*sn*-3-phosphoethanolamine-*N*-(lissamine rhodamine B sulfonyl) (rhodamine-PE) was obtained from Avanti Polar Lipids (Canada). Gd(III)DOTA–DSPE, Gd(III)DOTA–C6–DSPE and Gd(III)DTPA–bis(stearylamide) (Gd(III)DTPA–BSA) were synthesized by SyMO-Chem (Eindhoven, The Netherlands) and perfluoro-15-crown-5-ether was obtained from ABCR GmbH (Germany). All other commercial chemicals were purchased from Sigma-Aldrich in the highest available quality.

2.2. Emulsion preparation

Perfluorocarbon nanoparticles were composed of 20% (w/v) perfluoro-15-crown-5-ether and 2% (w/v) surfactant in THAM buffer (0.0252% w/v trishydroxymethyl aminomethane and 8.9 g L^{-1} NaCl, pH 7.4). The surfactant comprised DSPC, DSPE-PEG_{2000}, Gd(III)DOTA–DSPE/Gd(III)DOTA–C6–DSPE/Gd(III)DTPA–BSA, rhodamine-PE and cholesterol in a molar ratio of 1.55:0.15:0.3:0.003:1, while the composition of Gd-free nanoparticles consisted of DSPC, DSPE-PEG_{2000}, rhodamine-PE and cholesterol in a molar ratio of 1.85:0.15:0.003:1. In brief, 600 mmol total lipids were dissolved in 50 ml of a 2:1 v/v $CHCl_3$–MeOH mixture. Rhodamine-PE (0.1 mol%) was incorporated in the lipid monolayer as a fluorescent marker, although it was not utilized in the present study. The obtained solution was concentrated *in vacuo* at 10 mbar and 40 °C. The lipid film was dried overnight under a nitrogen flow to remove traces of organic solvents. Subsequently, the lipid film was heated to 70 °C and hydrated with 15 ml THAM buffer for 30 min. PFCE (4.5 g) was added to the lipid mixture and the crude emulsion was processed for 3 min in a high-pressure microfluidizer (M-110S, Microfluidics, USA) at 1500 bar, pre-heated to 70 °C and with the interaction chamber cooled with an ice bath. The final emulsion was cooled down in an ice bath for 5 min and stored in the dark at room temperature. The gadolinium-free emulsion was split into two batches; one of them was replenished with HPDO3A to come to an equal concentration of Gd to the gadolinium-containing samples (as determined by inductively coupled plasma atomic emission spectrometry (ICP-AES).

2.3. Characterization

Phospholipid concentrations of the liposomal dispersions were determined using Rouser *et al.* (19) and ICP-AES (DRCII, Perkin-Elmer, Philips Research Materials Analysis, Eindhoven, The Netherlands). Destruction of the samples was performed with nitric acid at 180 °C. In order to determine the longitudinal relaxivities, Gd(III) concentrations were determined using ICP-AES as well. The fluorine content was determined by high-field NMR spectroscopy.

The hydrodynamic radius and polydispersity of the emulsions were determined using dynamic light scattering (ALV/CGS-3 Compact Goniometer System, ALV-GmbH, Langen, Germany). Intensity correlation functions were measured at a scattering angle of $\theta = 90°$ using a wavelength of 632.8 nm. The diffusion coefficient (D) was obtained from cumulant fits of the intensity correlation function using ALV software. All reported hydrodynamic radii were calculated using the Stokes–Einstein equation, $r_h = kT/(6\pi\eta D)$, where k is the Boltzmann constant, T is the

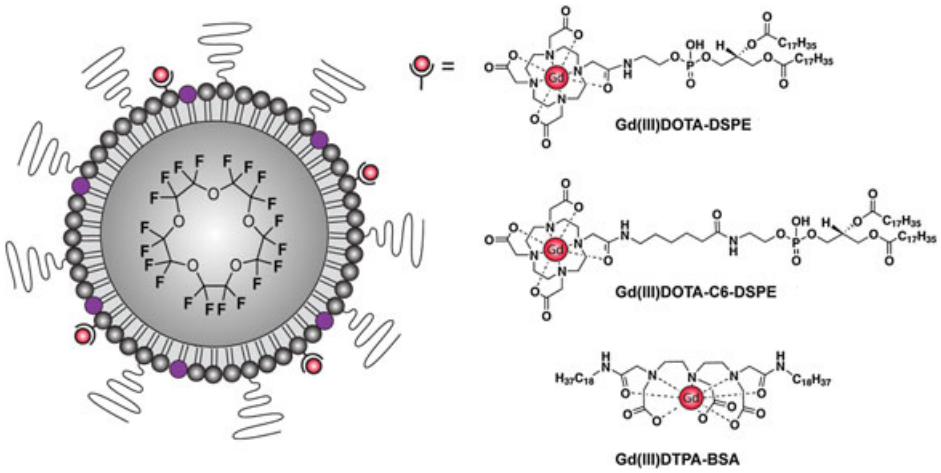

Figure 1. Schematic representation of a perfluoro-15-crown-5-ether (PFCE) emulsion with Gd(III)DOTA–DSPE, Gd(III)DOTA–C6–DSPE or Gd(III)DTPA–BSA as paramagnetic lipids on the surface of the nanoparticle monolayer. The magenta-colored symbols indicate the rhodamine-labeled lipids incorporated in the lipid monolayer.

absolute temperature and η is the solvent viscosity. Measurements were repeated five times and calculations were performed on the averaged correlation function of the five measurements.

The ζ-potential of the emulsions was determined with the microelectrophoretic method using the Malvern Zetasizer Nano ZS apparatus. Measurements were performed at 20 °C in THAM buffer (0.0252% w/v trishydroxymethyl aminomethane and 8.9 g L^{-1} NaCl) at pH 7.4. Each ζ-potential was an average of 1000 measurements.

Cryogenic transmission electron microscopy (cryo-TEM) pictures were obtained with a FEI TECNAI F30ST electron microscope operated at an accelerating voltage of 300 kV in low-dose mode. Samples for cryo-TEM were prepared by placing the emulsion (2 µL) on a 300-mesh carbon-coated copper grid and subsequently plunge-freezing this grid into liquid ethane using a Vitrobot.

2.4. ^{1}H nuclear magnetic relaxation dispersion

^{1}H nuclear magnetic relaxation dispersion (^{1}H NMRD) profiles were measured with a Stelar Spinmaster FFC-2000 fast-field cycling relaxometer (Mede, Italy) in a magnetic field range from 2.4×10^{-4} to 0.47 T (corresponding to proton Larmor frequencies of 0.01–20 MHz). Additional T_1 relaxation times were obtained with a Stelar SpinMaster Spectrometer [Stelar S.n.c., Mede (PV), Italy] equipped with a tunable probe (in the range 0.47–1.6 T), by means of the standard inversion recovery method with a 90° pulse width of 3.5 µs, using 16 experiments of four scans each. The T_1 reproducibility was within 5%. The temperature was controlled with a Stelar VTC-91 airflow heater equipped with a calibrated copper constantan thermocouple (precision of 0.1 °C). Measurements were performed at 25 and 37 °C. The longitudinal relaxivity r_1 was calculated taking into account the diamagnetic contributions of the buffer. The NMRD profiles at 25 °C were analyzed between 6 and 70 MHz according to the Solomon–Bloembergen–Morgan equations modified according to the Lipari–Szabo model free approach. The number of coordinating water molecules (q) was kept constant at $q = 1$. The global and local rotational correlation times (global and local τ_r), the correlation time for electronic relaxation (τ_v), the water residence lifetime (τ_m), the order parameter (S^2), the square of the transient of the zero field splitting of the electronic spin states (Δ^2), the water proton paramagnetic center distance (r), the distance of closest approach (a) and the diffusion coefficient (D) were allowed to vary.

2.5. Fluorine relaxation rates

Relaxation measurements ($^{19F}R_1$ and $^{19F}R_2$) were performed at five different field strengths (1.4, 3.0, 6.3, 9.4 and 14.0 T) at $T = 293$ K. The effect of nanoparticle concentration was assessed by evaluating a concentration-series of each emulsion formulation for their T_1 and T_2 values. The PFCE concentration of these samples was 3.8 mM, 22.5 mM, 43.2 mM, 0.45 M, 0.11 M, 0.22 M and 0.33 M as determined by magnetic resonance at 14.0 T using hexafluoropropanol as a reference. Protocols for $^{19F}R_1$and $^{19F}R_2$ were optimized for all field strengths and curves were fitted using a single-exponential decay function.

2.5.1. 1.4 T

The measurements at 1.4 T were performed according to Henoumont *et al*. (20). The longitudinal relaxation rate was monitored using a Bruker Minispec mq60 with a dedicated ^{19}F probe kindly provided by Bruker Optics (Delft, The Netherlands). An inversion recovery sequence with four averages was used. Ten inversion times ranging in an exponential fashion from 5 ms to at least 5 times the T_1 of the solution were used. The recycle delay was also set to at least 5 times the T_1 of the solution. For T_2, a Carr–Purcell–Meiboom–Gill (CPMG) NMR pulse sequence was performed, obtaining 2048 data points with at least 16 averages using $\tau = 1.0$ ms and a recycle delay of 7.0 s.

2.5.2. 3.0 T

Measurements at 3.0 T were conducted with a 3.0 T Philips Achieva clinical scanner (Philips Healthcare, Best, The Netherlands) equipped with a special design ^{1}H/^{19}F small bore coil. Longitudinal relaxation was measured by means of a single voxel spectroscopy sequence consisting of a 180° inversion pulse and a 90° excitation pulse, both wideband and tuned to the NMR offset of PFCE, and a sampling phase where the free induction

decay signal generated by the fluorine nuclei was acquired. The time interval between inversion and excitation was altered over a range from 1.5 ms to 10 s with 44 time points. The repetition time of the measurements was kept long, that is, 20 s, in order to ensure complete relaxation after each acquisition.

The measurements at 6.3 and 9.4 T were performed using two horizontal bore small animal scanners (Bruker Biospin, Ettlingen, Germany). Dedicated ^{19}F solenoid coils were used for experiments at 6.3 and 9.4 T. T_1 and T_2 measurements were performed using a rapid acquisition with relaxation enhancement (RARE) sequence with RARE factor 2, eight echo images [echo time (*TE*) 12–180 ms] and eight different repetition times (*TR*) of 375–5000 ms yielding saturation recovery times of 189–4814 ms. T_1 was determined by exponential fitting of the mean signal intensity vs the saturation recovery time in a region of interest (ROI) encompassing the entire sample, using only the first echo image (*TE* 12 ms). T_2 was determined by exponential fitting of the mean ROI signal intensity over all echo images at maximum *TR*.

2.5.3. 14.0 T

T_1 measurements at 14.0 T were performed using an inversion recovery NMR pulse sequence modified with magnetic-field gradients in order to suppress radiation damping. Inversion recovery curves (NMR signal intensity vs inversion recovery time) were calculated from the integrals of the PFCE ^{19}F-NMR signals. T_2 measurements were performed using a CPMG NMR pulse sequence. Decay curves (NMR signal intensity vs signal decay time) were calculated from the integrals of the PFCE ^{19}F-NMR signals. Actual T_1 and T_2 values were obtained from the inversion recovery curves and decay curves respectively, using the Levenberg–Marquard non-linear least-squares fitting procedure of the Bruker TOPSPIN NMR software.

3. RESULTS

3.1. Nanoparticle characterization

The sizes of FE–DOTA, FE–C6–DOTA, FE–DTPA, FE and FE + HPDO3A were 92.4 nm [polydispersity index (PDI) of 0.14], 97.3 nm (PDI 0.15), 87.1 nm (PDI 0.23), 87.3 nm (PDI 0.14) and 87.0 nm (PDI 0.11) in radius, respectively, as evidenced by dynamic light scattering measurements. Cryo-TEM revealed spherical nanoparticles with an electron-dense core that can be attributed to the high concentration of PFCE (Fig. 2). Liposomes were observed in some cases, although the number was estimated to be <3% of the total amount of nanoparticles.

Phospholipid concentration was 37 ± 4 mM for all samples and gadolinium content of the gadolinium-containing emulsions (including FE + HPDO3A) was 2.2 ± 0.1 mM as determined by ICP-AES. ζ-Potential measurements revealed a surface charge close to zero (−2.0–0 mV) for all nanoparticle formulations.

3.2. ^{1}H NMRD

^{1}H NMRD profiles for the Gd(III) complexes of FE–DOTA, the FE–C6–DOTA and FE–DTPA ligands were measured at 25 and 37 °C (Fig. 3). At 1.41 T, a field close to the typical clinical imaging field strength, the longitudinal relaxivities r_1 at 25 °C were 34.6, 35.9 and 8.9 $mM^{-1} s^{-1}$, respectively. The longitudinal relaxivities are the average ionic relaxivities of the Gd(III) ions on the lipid surface.

The relaxivity per emulsion droplet is much higher as one emulsion typically contains 40 000 Gd(III) ions, based on a calculation of an emulsion with a diameter of 200 nm and a lipid surface area of 0.6 nm^2. The peaks in the NMRD profiles observable around 30 MHz are indicative of a restricted rotational motion of the Gd(III) centers, which is expected for the complexes that are embedded in the particle surface. It is noteworthy that the peak relaxivity for the FE–DTPA-based emulsion is much less pronounced than the two DOTA-like complexes. The profiles were analysed using the standard Solomon–Bloembergen–Morgan (SBM) relaxation model (21,22), properly modified using the model-free Lipari–Szabo approach (hereafter LS–SBM) that takes into account the occurrence of a local fast rotation of the metal coordination cage of the complex superimposed on the slower global motion of the nanoparticle (23). The relative contribution of the two motions is defined by the order parameter S^2 ($0 \le S^2 \le 1$) that is equal to 0 in presence of local motion only, and equal to 1 in absence of local motion. Owing to the lack of an adequate theory for describing the low field relaxivity of slowly tumbling paramagnetic complexes, data were analyzed in the high field portion only (6–70 MHz, Fig. 4) (20,24,25). The estimated parameters presented in Table 1 were the result of the application of the LS–SBM model.

The main difference among the three samples is represented by the much longer (approximately one order of magnitude) residence lifetime of the Gd(III)-bound water molecule for the bis-amide derivative FE–DTPA (2.03 μs) as compared with FE–DOTA and FE–C6–DOTA, whose τ_M values (155 and 190 ns, respectively) are slightly lower than those reported for their water-soluble counterparts GdDTPA and GdDOTA. The local and global rotational tumbling values are rather similar for FE–DTPA, FE–DOTA and FE–C6–DOTA (100–120 ps and 3.5–5.0 ns, respectively) and are consistent with amphiphilic Gd(III) complexes incorporated in soft nanoparticles (26,27). Interestingly, the S^2 values obtained were similar among the complexes and quite high (0.88–0.95), thereby indicating a good coupling between the rotation of the coordination cage of the complexes and the global motion of the nanoemulsion.

3.3. Fluorine relaxation rates

In order to study the relationship of gadolinium construct and the $^{19F}R_1$ and $^{19F}R_2$ at different field strengths, five different fluorine emulsions were measured at 1.4, 3.0, 6.3, 9.4 and 14.0 T. Three emulsions FE–DOTA, FE–C6–DOTA FE–DTPA contained paramagnetic gadolinium ion Gd(III) in the lipid layer, while two emulsions FE and FE + HPDO3A (a PFCE emulsion with HPDO3A in the aqueous solution) served as controls.

All emulsions were measured in a concentration series of at least five different nanoparticle concentrations. No significant differences in $^{19F}R_1$ were observed for different concentrations (data not shown) and these were used to compute the average $^{19F}R_1$ and its standard deviations. These $^{19F}R_1$ values of the five emulsions as a dependence on the magnetic field can be observed in Fig. 5.

Upon higher field strengths, the $^{19F}R_1$ of FE increased going from $0.89 \pm 0.02\ s^{-1}$ at 1.4 T to $1.49 \pm 0.03\ s^{-1}$ at 14.0 T. The relationship between $^{19F}R_1$ and magnetic field (B) can be described in a linear fit as $^{19F}R_1 = 0.046*B + 0.85\ s^{-1}$, $R^2 = 0.98$. Adding HPDO3A to the aqueous solution did not alter the longitudinal relaxation of fluorine as compared with FE and a similar linear behavior can be observed with $^{19F}R_1 = 0.045*B + 0.85\ s^{-1}$, $R^2 = 0.99$. Moreover, pure PFCE measured at these field strengths

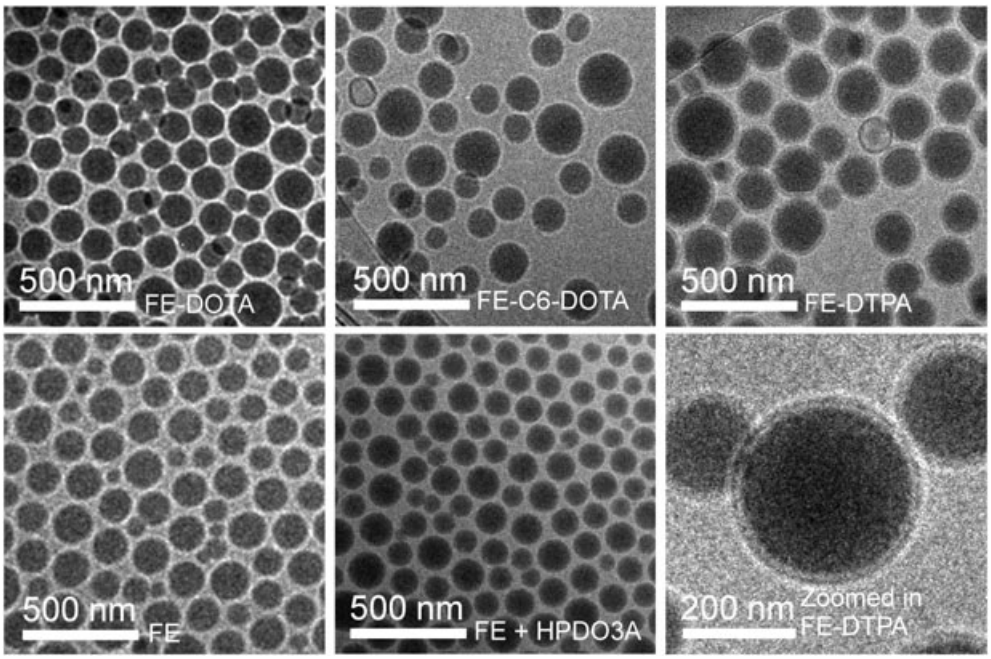

Figure 2. Cryo-TEM images of the five PFCE emulsions show nanoparticles with sizes of around 180 nm in diameter. The last sample (FE–DTPA) at a higher magnification shows the paramagnetic lipid monolayer of the PFCE nanoparticle.

resulted in $^{19F}R_1$ values similar to that of FE and FE + HPDO3A (data not shown). The effect of gadolinium incorporated in the lipid layer of the emulsion on $^{19F}R_1$ was pronounced especially in the lower field region. FE–DOTA as well as FE–C6–DOTA showed increased $^{19F}R_1$ values as compared with FE at 1.4 T (1.05 ± 0.10 and $1.02 \pm 0.05\ s^{-1}$, respectively, vs $0.89 \pm 0.02\ s^{-1}$), but were also statistically significant higher at 3.0 T (1.07 ± 0.02 and $1.08 \pm 0.01\ s^{-1}$ vs $1.02 \pm 0.02\ s^{-1}$), although the differences were less prominent than at 1.4 T. The increase in $^{19F}R_1$ of FE–DOTA and FE–C6–DOTA with increasing field strengths was minor in the lower field region (<6 T) and became at fields ≥ 6.3 T identical to that of FE. Thus, at high field strengths, Gd no longer has an effect on the longitudinal relaxation rate of fluorine.

The strongest benefit of including gadolinium in a fluorine emulsion for ^{19}F imaging can be observed for FE–DTPA. The $^{19F}R_1$ of FE–DTPA of $1.45 \pm 0.04\ s^{-1}$ was much higher than that of FE or the DOTA-functionalized nanoparticles at 1.4 T and comparable to its $^{19F}R_1$ at 14 T ($1.50 \pm 0.02\ s^{-1}$). At 3.0 T the $^{19F}R_1$ dropped to $1.15 \pm 0.04\ s^{-1}$ but remained statistically higher than that of FE or FE–DOTA. The minimum $^{19F}R_1$ value for FE–DTPA was found at a magnetic field of 6.3 T ($1.13 \pm 0.02\ s^{-1}$) and from that point increased with similar values for $^{19F}R_1$ as FE.

Transversal relaxation rates $^{19F}R_2$ were measured for gadolinium-functionalized PFCE nanoparticles and its controls. $^{19F}R_2$ values decreased with a lower concentration of emulsion. Therefore, for a good comparison, only the values measured with the highest concentration sample are shown (0.45 M PFCE). There was an increase in $^{19F}R_2$ for the gadolinium-functionalized emulsions, as can be observed in Fig. 6A. Especially for higher fields, this increase in R_2 can reach a factor of 25-fold compared with non-functionalized emulsions. Taking a closer look at FE and FE + HPDO3A, a similar increase in $^{19F}R_2$ upon higher fields is observed, although to a much smaller extent (Fig. 6B).

To visualize in more detail the effect of gadolinium on the fluorine relaxation, the ratio between $^{19F}R_2$ and $^{19F}R_1$ ratio was plotted against the magnetic field (Fig. 7). For FE and FE + HPDO3A, the $^{19F}R_2/R_1$ ratio increased only slightly with increasing field strengths. However, for the gadolinium-functionalized emulsions $^{19F}R_2/R_1$ ratio increased strongly. At 3.0 T, measured $^{19F}R_2/R_1$ ratios reached levels >5–10, indicating a severe influence of $^{19F}R_2$ effects. The $^{19F}R_2/R_1$ ratio increased to 58 for 14.0 T, while for FE, the $^{19F}R_2/R_1$ ratio at 14.0 T was only 2.2.

4. DISCUSSION

Two macrocyclic gadolinium-functionalized lipids [Gd(III)DOTA–DSPE, Gd(III)DOTA–C6–DSPE] and one linear gadolinium-functionalized lipid [Gd(III)DTPA–BSA] were investigated for their capability to increase the fluorine relaxation rates of PFCE emulsions to generate a higher signal-to-noise ratio per unit time from the ^{19}F nuclei. Neubauer *et al.* previously demonstrated that a Gd–DTPA chelate increases the $^{19F}R_1$, despite the hydrophilic nature of the gadolinium-chelate, which reduces the chances of interaction of gadolinium with the perfluorocarbon core (12). Here, we investigated whether macrocyclic chelates are favorable to increasing the relaxivity of $^{19F}R_1$. This might become clinically relevant with respect to Gd-induced toxicity and NSF as Gd–DOTA chelates are known for their higher Gd binding affinity as compared with Gd–DTPA–bisamides, resulting in lower chances of inducing the development of NSF.

4.1. NMRD measurements

^{1}H NMRD curves were measured for the gadolinium-functionalized constructs to investigate the efficiency of the paramagnetic nanoemulsions to generate MRI contrast at different magnetic field strengths. The two emulsions based on Gd(III) DOTA-like amphiphiles showed a significantly increased longitudinal relaxivity compared with the Gd(III)DTPA–BSA-containing emulsion. The peaks in the NMRD profiles around 30 MHz are characteristic for macromolecular complexes, as was also observed for gadolinium-functionalized liposomal MR contrast

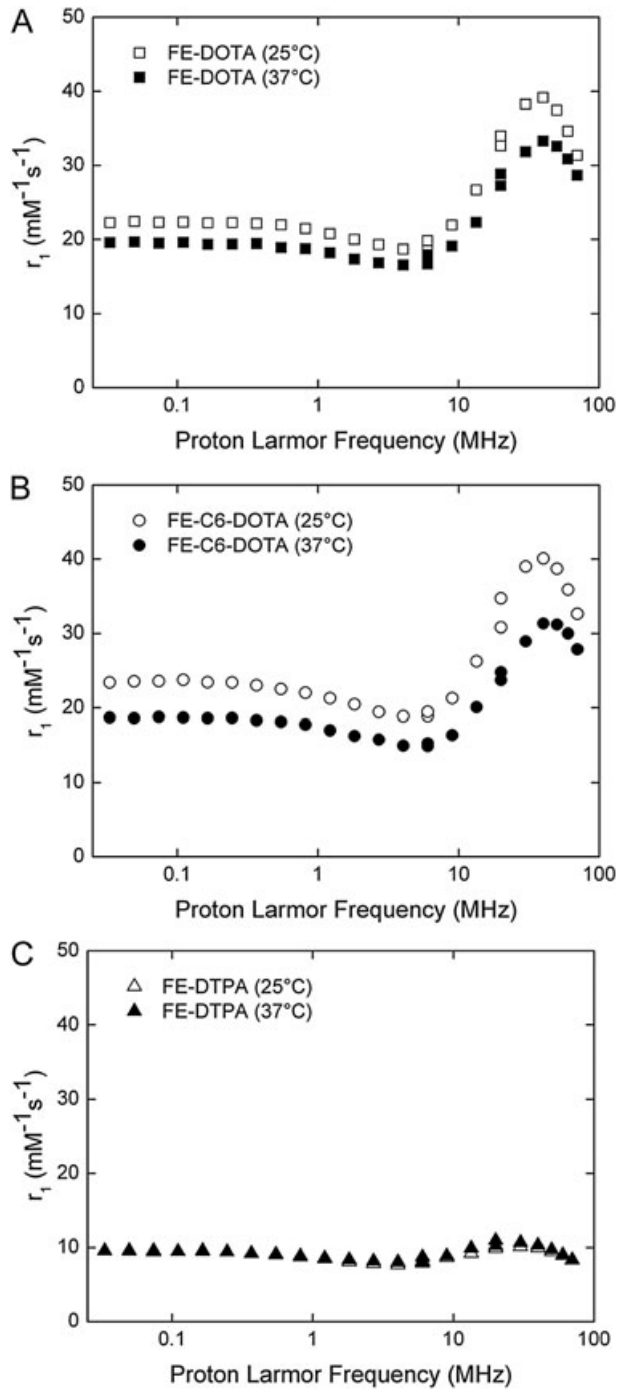

Figure 3. ^{1}H-NMRD profiles of (A) FE–DOTA; (B) FE–C6–DOTA; and (C) FE–DTPA measured at 25 and 37 °C.

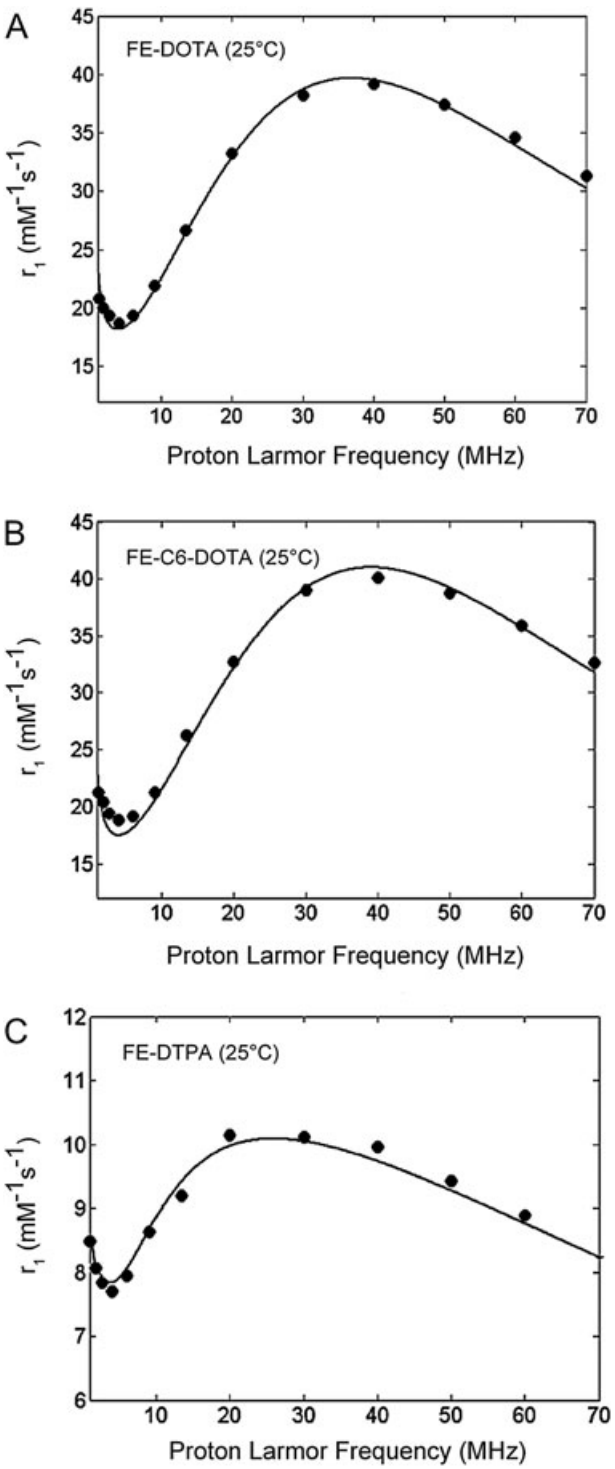

Figure 4. Fits of ^{1}H-NMRD profiles of (A) FE–DOTA; (B) FE–C6–DOTA; and (C) FE–DTPA at 25 °C in the magnetic high field range of 1–70 MHz.

agents (26,27). Using the LS–SBM model, estimations of the parameters controlling the electronic relaxation times, Δ^2 and τ_V, the local (τ_{Rloc}) and global (τ_{Rglob}) rotational correlation times, the order parameter, S^2, and the residence lifetime of the Gd(III)-bound water molecule τ_M, can be made. Both of the rotational motions occur with similar timescales (100–120 ps for τ_{Rloc} and 3.5–5.0 ns for τ_{Rglob}) for all of the complexes, and S^2 values are also very close (0.88–0.95), thereby indicating that all the incorporated complexes are tightly bound to the nanoemulsion surface.

The main difference between the macrocyclic (DOTA-like) and the linear (DTPA-like) chelates primarily resides, as expected, in the parameters controlling the electronic relaxation times. In fact, it is well established that the more rigid cyclic cage is characterized by smaller Δ^2 and τ_V values (corresponding to a long electronic relaxation time) than the structurally more dynamic linear cage.

Another relevant difference among the investigated complexes is represented by the water residence lifetime. The τ_M values for FE–DOTA and FE–C6–DOTA are similar and only slightly lower to the values reported for the parent

Table 1. Best fitting values of the electronic relaxation times Δ^2 and τ_V, the local (τ_{Rloc}) and global (τ_{Rglob}) rotational correlation times, the residence lifetime of the Gd(III)-bound water molecule τ_M and the superimposition grade between the two tumbling motions S^2, obtained from fitting the LS–SBM model at high frequencies (6–70 MHz)

	FE–DOTA	FE–C6–DOTA	FE–DTPA
Δ^2 ($\times 10^9$)	1.4	1.6	2.4
τ_V (ps)	13.2	11.5	40
$\tau_{R\ local}$ (ps)	120	110	100
$\tau_{R\ global}$ (ps)	3.5	3.8	5
τ_M (ns)	190	155	2030
S^2	0.95	0.92	0.88

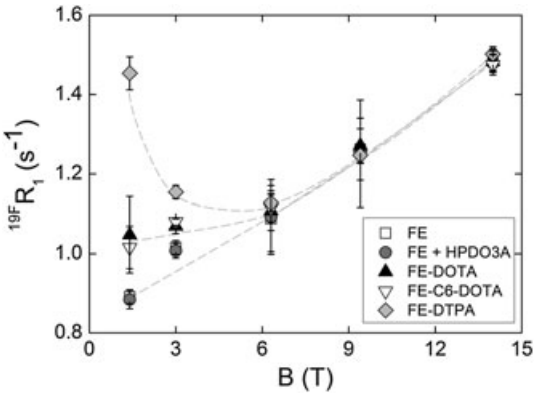

Figure 5. $^{19F}R_1$ (s^{-1}) measured for fluorine emulsions (FE), FE + HPDO3A, FE–DOTA, FE–C6–DOTA and FE–DTPA at different field strengths. A general increase in $^{19F}R_1$ is observed for higher field strengths with FE–DTPA having the most prominent influence of the gadolinium construct on $^{19F}R_1$. Data represent means ± SD ($n = 5$). The dashed lines are guides to the eye.

tetracarboxylic Gd–DOTA (250 ns) (28). However, it is typically observed that the transformation of a metal coordinating carboxylate to a carboxoamide moiety causes a τ_M elongation primarily owing to the reduction of the negative overall charge of the chelate, but the amphiphilic macrocyclic complexes herein studied do not fulfil such an expectation. This finding could reflect an interaction occurring between the inner-sphere water and its molecular environment at the hydration shell of the particle that can somehow accelerate the exchange rate. Second-sphere effects on the Gd(III)-bound water molecule have already been reported (29). A further support to this view can be derived from the observation that, despite the presence of the rotationally flexible C6 linker, the S^2 value of FE–C6–GdDOTA complex is not smaller than those of the other two agents.

As far the amphiphilic FE–DTPA complex is concerned, it is important to recall that it is a *bis*-amide derivative of Gd-DTPA and, as such, it shows a very long residence lifetime (2.03 μs).

The occurrence of a long residence lifetime for this species is also indicated by the temperature dependence of the relaxivity shown in Fig. 3. In fact, when τ_M is comparable to or exceeds the relaxation time of the water protons coordinated to the Gd (III) center, the relaxivity is limited by the exchange process and, consequently, a shortening of τ_M (as happens upon heating) leads to a relaxivity enhancement or, as in this case, to a very reduced temperature effect on the relaxivity (Fig. 3). It is noteworthy that similar observations were previously reported by Winter *et al*. and Hak *et al*. (17,18).

4.2. Relaxivity measurements of fluorine

$^{19F}R_1$ and $^{19F}R_2$ measurements were performed at five different field strengths to determine the effect of three different paramagnetic lipids on the fluorine signal. An increase in $^{19F}R_1$ was observed with increasing magnetic fields for FE, FE + HPDO3A and for pure PFCE, a behavior also observed in other studies (11,12). This increase is probably related to the field dependence of the chemical-shift anisotropy relaxation mechanism as described by Shukla *et al*. (30). Moreover, $^{19F}R_1$ values were similar at each individual field strength, indicating that the encapsulation of fluorine into a nanoparticle, and in addition adding HPDO3A to the aqueous solution, does not influence the fluorine relaxation rate. FE–DOTA and FE–C6–DOTA had significantly increased $^{19F}R_1$ values at 1.4 and 3.0 T, but followed a similar trend to FE for higher field strengths. This behavior was even more apparent for FE–DTPA, showing an increase in $^{19F}R_1$ of a factor of 1.6 using only 10 mol% of Gd(III)DTPA–BSA in the lipid monolayer. The effect was strongest for 1.4 T and was much reduced for 3.0 T to follow at higher field strengths a similar trend as for FE. A possible explanation for the stronger effect of Gd(III)DTPA–BSA as compared with the paramagnetic DOTA–lipids can be found in the position of the chelate relative to the lipid monolayer. Using the LS–SBM model, relatively high water residency times were found for Gd(III)DTPA, indicating a lesser

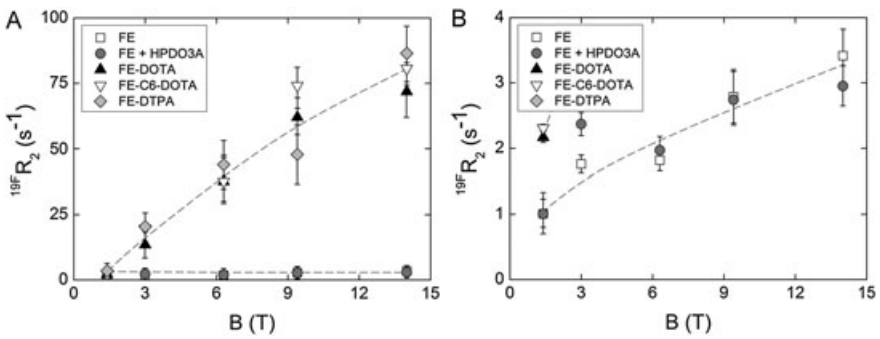

Figure 6. $^{19F}R_2$ (s^{-1}) measured for FE, FE + HPDO3A, FE–DOTA, FE–C6–DOTA and FE–DTPA at different field strengths. An increase in $^{19F}R_2$ is observed for higher magnetic fields especially for the gadolinium-functionalized emulsions (A), but can also be observed for FE and FE + HPDO3A (B: zoom of A). Data represent means ± SD ($n = 5$). The dashed lines are guides to the eye.

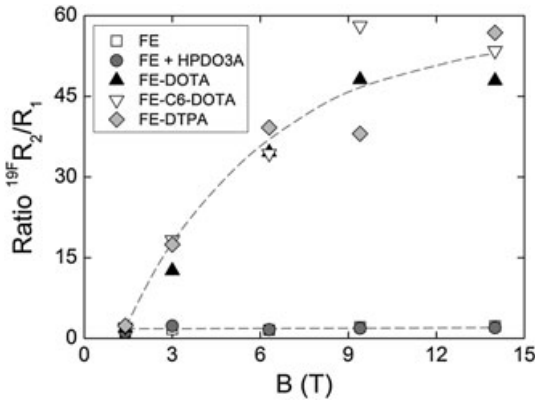

Figure 7. $^{19F}R_2/R_1$ as a function of the magnetic field. The dashed lines are guides to the eye.

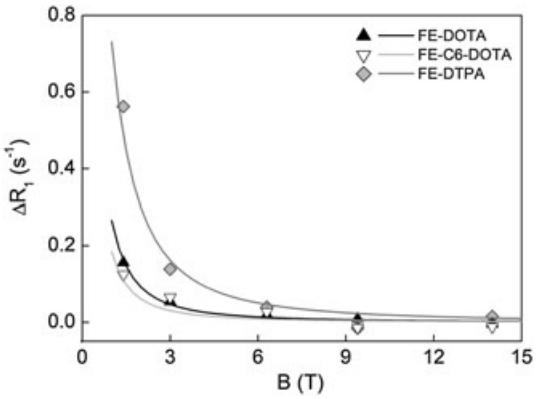

Figure 8. Relaxation enhancement $^{19F}R_1$ caused by gadolinium upon different magnetic fields, extracted from experimental data (symbols) and from the model prediction (lines) of FE–DOTA, FE–C6–DOTA and FE–DTPA.

access to free water molecules compared with the Gd(III)DOTA constructs. This indicates that the Gd(III)DTPA is positioned closer to the nanoparticle core and thus in closer proximity to fluorine atoms inside the emulsion compared with the Gd(III)DOTA construct, and therefore shows a more pronounced influence on the relaxation rate. The most efficient $^{19F}R_1$ increase was observed at lower field strengths, which can be caused by a better matching to the Larmor frequency of the nucleus (12,31).

Transversal relaxation rates of FE and FE + HPDO3A showed only a minor increase upon higher field strengths. For FE–DOTA an increased $^{19F}R_2$ was observed, which was further enhanced withhigher magnetic fields. FE–C6–DOTA and FE–DTPA showed a similar behavior to FE–DOTA. The reason why the DOTA constructs have a more pronounced influence on $^{19F}R_2$ as compared with $^{19F}R_1$ could be due to the fact that T_2 effects generally extend over longer distances than T_1. For the paramagnetic samples, T_2 values were very short, causing a relatively large variation on the measurement data. Nonetheless, data from Fig. 5 suggest a clear lanthanide-induced fluorine relaxivity that should be taken into account before imaging as it influences the $^{19F}R_2/R_1$ ratio. Figure 6 indicates that the ratio $^{19F}R_2/R_1$ for FE and FE + HPDO3A increases slightly upon higher field strengths but this is only minor when we compare it with the increase in the $^{19F}R_2/R_1$ ratio for perfluorinated nanoparticles with paramagnetic lipids included in the lipid monolayer. This graph shows that for many applications it is not advantageous for the signal-to-noise-ratio of fluorine to incorporate paramagnetic lipids, especially at high field strengths, but also already severely influences the $^{19F}R_1$ at 1.4 T. However, some applications would benefit from paramagnetic lipids on the nanoparticle surface as they enhance the ^{1}H relaxation rate.

Recently, a physical model was developed to understand the longitudinal ^{19}F relaxation enhancement by Gd^{3+} in perfluorocarbon emulsions (13). Briefly, the model describes the influence of Gd^{3+} on the $^{19F}R_1$ by an outer-sphere relaxation mechanism, since the distance between gadolinium and fluorine is at least the distance of one hydrophobic tail (~1.5 nm). We applied the model of Hu *et al.* (13) to describe the field dependence of the increase in $^{19F}R_1$ by the incorporation of Gd^{3+}-containing chelates in our PFCE nanoparticles, as shown in Fig. 8. Model (solid lines) and data (symbols) are in good agreement using estimates of the distance of the closest approach between Gd^{3+} and ^{19}F of $d = 2.0$, 2.2 and 1.5 nm for FE–DOTA, FE–C6–DOTA and FE–DTPA, respectively, while keeping all other model parameters constant. The value for FE–DTPA is higher than the one found by Hu *et al.* ($d = 0.9$ nm), which might be explained by the fact that we use 10 mol% Gd-DTPA–BSA in the lipid monolayer compared with 30 mol% of Gd-DTPA–BOA. Our particles were also slightly larger (87 nm in radius compared with 75 nm), which could explain the overall lower increase in R_1, as the influence of Gd on $^{19F}R_1$ scales with 1/particle radius, related to the surface to volume ratio.

In this study, we showed the influence of three gadolinium–lipids on the water proton relaxivities and fluorine relaxation rates $^{19F}R_1$ and $^{19F}R_2$ of a PFCE nanoparticle at 1.4, 3.0, 6.3, 9.4 and 14.0 T. Gd(III)DOTA–DSPE and Gd(III)DOTA–C6–DSPE are favorable as contrast agents for proton NMR, but the opposite holds for Gd(III)DTPA–BSA, which showed the highest increase in $^{19F}R_1$, possibly owing to its closer proximity to the fluorinated nanoparticle core as compared with the Gd(III)DOTA-constructs. For clinical applications this will result in a trade-off between the signal-to-noise ratio of fluorine and that of proton, which will depend mostly on its exact application. Nonetheless, our data clearly show that, for gadolinium-functionalized perfluorocarbon nanoparticles, the current clinical field strengths (1.5–3.0 T) are favorable for fluorine imaging as increased $^{19F}R_1$ values are observed. For higher field strengths in the range of 6.3–9.4 T, gadolinium is a disadvantage as it does not increase the $^{19F}R_1$ as compared with emulsions without gadolinium, but does significantly increase the $^{19F}R_2$. For the standard emulsions without gadolinium, the use of higher field strengths (14.0 T) is favorable as high $^{19F}R_1$ values can be obtained in combination with low $^{19F}R_2$ values. Our data suggest that the most favorable situation for fluorine measurements is at high magnetic fields without the inclusion of gadolinium constructs.

Acknowledgments

We kindly acknowledge Larry de Graaf for building a dedicated ^{19}F solenoid coil, Dr Marcel Verheijen for performing cryo-TEM analysis and Danielle Beelen for her help on the 14.0 T measurements. We thank Dr L. Hu and professor S. A. Wickline for help with the physical modeling of the field dependence of the Gd-induced relaxation enhancement. This research was performed within the framework of CTMM, the Center for Translational Molecular Medicine (www.ctmm.nl), project PARISK (grant 01C-202), and supported by The Netherlands Heart Foundation.

REFERENCES

1. Morawski AM, Winter PM, Yu X, Fuhrhop RW, Scott MJ, Hockett F, *et al*. Quantitative 'magnetic resonance immunohistochemistry' with ligand-targeted (19)F nanoparticles. Magn Reson Med 2004; 52: 1255–1262; doi: 10.1002/mrm.20287
2. Waters EA, Chen J, Allen JS, Zhang H, Lanza GM, Wickline SA. Detection and quantification of angiogenesis in experimental valve disease with integrin-targeted nanoparticles and 19-fluorine MRI/MRS. J Cardiovasc Magn Reson 2008; 10: 43.
3. Southworth R, Kaneda M, Chen J, Zhang L, Zhang H, Yang X, *et al*. Renal vascular inflammation induced by Western diet in ApoE-null mice quantified by (19)F NMR of VCAM-1 targeted nanobeacons. Nanomedicine 2009; 5: 359–367.
4. Ruiz-Cabello J, Walczak P, Kedziorek DA, Chacko VP, Schmieder AH, Wickline SA, *et al*. In vivo 'hot spot' MR imaging of neural stem cells using fluorinated nanoparticles. Magn Reson Med 2008; 60: 1506–1511.
5. Srinivas M, Morel PA, Ernst LA, Laidlaw DH, Ahrens ET. Fluorine-19 MRI for visualization and quantification of cell migration in a diabetes model. Magn Reson Med 2007; 58: 725–734.
6. Srinivas M, Turner MS, Janjic JM, Morel PA, Laidlaw DH, Ahrens ET. In vivo cytometry of antigen-specific T cells using 19F MRI. Magn Reson Med 2009; 62: 747–753.
7. Janjic JM, Ahrens ET. Fluorine-containing nanoemulsions for MRI cell tracking. Wiley Interdiscip Rev Nanomed Nanobiotechnol 2009; 1: 492–501.
8. Mason RP, Antich PP, Babcock EE, Gerberich JL, Nunnally RL. Perfluorocarbon imaging in vivo: a 19F MRI study in tumor-bearing mice. Magn Reson Imag 1989; 7: 475–485.
9. Kadayakkara DK, Janjic JM, Pusateri LK, Young WB, Ahrens ET. In vivo observation of intracellular oximetry in perfluorocarbon-labeled glioma cells and chemotherapeutic response in the CNS using fluorine-19 MRI. Magn Reson Med 2010; 64: 1252–1259.
10. Ratner AV, Quay S, Muller HH, Simpson BB, Hurd R, Young SW. 19F relaxation rate enhancement and frequency shift with Gd-DTPA. Invest Radiol 1989; 24: 224–227.
11. Chalmers KH, De Luca E, Hogg NH, Kenwright AM, Kuprov I, Parker D, *et al*. Design principles and theory of paramagnetic fluorine-labelled lanthanide complexes as probes for (19)F magnetic resonance: a proof-of-concept study. Chemistry 2010; 16: 134–148.
12. Neubauer AM, Myerson J, Caruthers SD, Hockett FD, Winter PM, Chen J, *et al*. Gadolinium-modulated 19F signals from perfluorocarbon nanoparticles as a new strategy for molecular imaging. Magn Reson Med 2008; 60: 1066–1072.
13. Hu L, Zhang L, Chen J, Lanza GM, Wickline SA. Diffusional mechanisms augment the fluorine MR relaxation in paramagnetic perfluorocarbon nanoparticles that provides a 'relaxation switch' for detecting cellular endosomal activation. J Magn Reson Imag 2011; 34: 653–661.
14. Kuo PH, Kanal E, Abu-Alfa AK, Cowper SE. Gadolinium-based MR contrast agents and nephrogenic systemic fibrosis. Radiology 2007; 242: 647–649.
15. Stratta P, Canavese C, Aime S. Gadolinium-enhanced magnetic resonance imaging, renal failure and nephrogenic systemic fibrosis/nephrogenic fibrosing dermopathy. Curr Med Chem 2008; 15: 1229–1235.
16. Aime S, Caravan P. Biodistribution of gadolinium-based contrast agents, including gadolinium deposition. J Magn Reson Imag 2009; 30: 1259–1267.
17. Winter PM, Athey P, Kiefer G, Gulyas G, Frank K, Fuhrhop R, *et al*. Improved paramagnetic chelate for molecular imaging with MRI. J Magn Magn Mater 2005; 293: 540–545.
18. Hak S, Sanders HM, Agrawal P, Langereis S, Grull H, Keizer HM, *et al*. A high relaxivity Gd(III)DOTA-DSPE-based liposomal contrast agent for magnetic resonance imaging. Eur J Pharm Biopharm 2009; 72: 397–404.
19. Rouser G, Fleischer S, Yamamoto A. Two dimensional thin layer chromatographic separation of polar lipids and determination of phospholipids by phosphorus analysis of spots. Lipids 1970; 5: 494–496.
20. Henoumont C, Laurent S, Vander Elst L. How to perform accurate and reliable measurements of longitudinal and transverse relaxation times of MRI contrast media in aqueous solutions. Contrast Media Mol Imag 2009; 4: 312–321.
21. Morgan LO, Nolle AW. Proton spin relaxation in aqueous solutions of paramagnetic ions. II. Cr^{+++}, Mn^{++}, Ni^{++}, Cu^{++}, and Gd^{+++}. J Chem Phys 1959; 31: 365
22. Freed JH. Dynamic effects of pair correlation functions on spin relaxation by translational diffusion in liquids. II. Finite jumps and independent T1 processes. J Chem Phys 1978; 68: 4034–4037
23. Woessner DE. Nuclear spin relaxation in ellipsoids undergoing rotational brownian motion. J Chem Phys 1962; 37(3): 647–654
24. Troughton JS, Greenfield MT, Greenwood JM, Dumas S, Wiethoff AJ, Wang J, *et al*. Synthesis and evaluation of a high relaxivity manganese(II)-based MRI contrast agent. Inorg Chem 2004; 43: 6313–6323.
25. Zhang Z, Greenfield MT, Spiller M, McMurry TJ, Lauffer RB, Caravan P. Multilocus binding increases the relaxivity of protein-bound MRI contrast agents. Angew Chem Int Ed Engl 2005; 44: 6766–6769.
26. Strijkers GJ, Mulder WJ, van Heeswijk RB, Frederik PM, Bomans P, Magusin PC, Nicolay K. Relaxivity of liposomal paramagnetic MRI contrast agents. MAGMA 2005; 18: 186–192.
27. Kielar F, Tei L, Terreno E, Botta M. Large relaxivity enhancement of paramagnetic lipid nanoparticles by restricting the local motions of the GdIII chelates. J Am Chem Soc 2010; 132: 7836–7837.
28. Caravan P, Ellison JJ, McMurry TJ, Lauffer RB. Gadolinium(III) chelates as MRI contrast agents: structure, dynamics, and applications. Chem Rev 1999; 99: 2293–2352.
29. Jacques V, Dumas S, Sun WC, Troughton JS, Greenfield MT, Caravan P. High-relaxivity magnetic resonance imaging contrast agents. Part 2. Optimization of inner- and second-sphere relaxivity. Invest Radiol 2010; 45: 613–624.
30. Shukla HP, Mason RP, Woessner DE, Antich PP. A comparison of three commercial perfluorocarbon emulsions as high-field 19F NMR probes of oxygen tension and temperature. J Magn Reson Ser B 1995; 106: 131–141.
31. Koenig SH, Brown RD 3rd. Relaxation of solvent protons by paramagnetic ions and its dependence on magnetic field and chemical environment: implications for NMR imaging. Magn Reson Med 1984; 1: 478–495.